Journal of Intelligent Material Systems and Structures

Original Article

Journal of Intelligent Material Systems and Structures
2018, Vol. 29(13) 2823–2839

DOI: 10.1177/1045389X18781023
journals.sagepub.com/home/jim
SAGE

Analysis of a multi-axial quantum informed ferroelectric continuum model: Part 1—uncertainty quantification

Paul Miles[1], Lider Leon[1], Ralph C Smith[1] and William S Oates[2]

Abstract

The uncertainty of phenomenological parameters governing fourth- and sixth-order Landau energy functions and electrostrictive coupling of ferroelectric single crystals is analyzed for lead titanate. Bayesian statistics are used to quantify model parameter uncertainty associated with approximating lattice strain and full-field electron density from density functional theory calculations as a homogenized, electromechanical continuum. The continuum model parameter uncertainty is propagated through the model to obtain prediction and credible intervals when estimating the non-convex energy surface and electrostrictive stresses for lead titanate. The results illustrate the important differences in fourth- and sixth-order Landau energy functions that influence estimations of the crystal phase. In addition, Bayesian statistics provides important insights into varying degrees of uncertainty along different thermodynamic paths associated with polarization rotation versus polarization changes along its spontaneous direction. Methods to reduce this uncertainty via decoupling electromechanical relations are demonstrated. The results provide critical insight into the development of self-consistent models that utilize density functional theory for large-scale continuum model simulations. Furthermore, the results are complementary to Part 2, in which we develop and apply new concepts in model parameter global sensitivity to accelerate uncertainty quantification of correlated parameters using higher order energy functions for a broad range of ferroic materials.

Keywords

Ferroelectric, density functional theory, Landau energy, uncertainty analysis, Bayesian inference

Introduction

Ferroelectric materials critically impact a variety of adaptive structures and intelligent systems including energy harvesting circuits, structural health monitoring sensors, and flow control actuators (Cattafesta and Sheplak, 2011; Jaffe, 2012; Lines and Glass, 1977; Smith, 2005). Their pervasive use in smart structures and adaptive systems motivates the need for methodologies that accurately judge models across scales to accelerate materials discovery, development, and future applications. Numerous ferroelectric constitutive models have been developed and range from macroscale phenomenological models (Huber et al., 1999), microscale models (Su and Landis, 2007), coupling with atomistic relations (Kowalewsky, 2004; Völker et al., 2011), to *ab initio* calculations (Cohen, 1992; King-Smith and Vanderbilt, 1994; Vanderbilt, 2004). Whereas models exist that couple length scales, the approach to homogenize and speed up calculations undoubtedly results in loss of information. This uncertainty can drastically vary depending upon the quantum degrees of freedom that are approximated at the atomistic or continuum scale. Here we explore these effects by investigating methods to approximate internal electronic degrees of freedom, their corresponding atomic evolution, and continuum electromechanics

[1]Department of Mathematics, North Carolina State University, Raleigh, NC, USA
[2]Florida Center for Advanced Aero-Propulsion (FCAAP), Aero-Propulsion, Mechatronics and Energy (AME) Center, Department of Mechanical Engineering, Florida A&M and Florida State University, Tallahassee, FL, USA

Corresponding author:
William S Oates, Florida Center for Advanced Aero-Propulsion (FCAAP), Aero-Propulsion, Mechatronics and Energy (AME) Center, Department of Mechanical Engineering, Florida A&M and Florida State University, 2003 Levy Ave., Tallahassee, FL 32310, USA.
Email: woates@eng.famu.fsu.edu

under three-dimensional (3D) deformation in a ferroelectric single crystal.

Whereas density functional theory (DFT) can accurately quantify many structure–property relations in solids (Gonze et al., 2009; Payne et al., 1992), development of large-scale computations that can model polarization evolution and electrostriction while accurately accounting for the underlying atomic and electronic structural evolution remains challenging. Continuum approximations of electronic behavior during complex lattice distortions can lead to parameter uncertainty as the polarization evolves along different thermodynamic paths from applied electric fields and stress (Frederiksen et al., 2004; Hu et al., 2014; Oates, 2014; Smith, 2013).

The analysis presented here employs Bayesian inference, which provides a method to estimate unknown phenomenological parameters with uncertainty instead of optimization of a fixed set of material parameters. In the present case, this uncertainty is associated with the homogenization of DFT energy and stress calculations over a range of polarization values that define the 3D energy landscape and electrostrictive coupling. The continuum approximation results in a reduction of the internal degrees of freedom of atomic position and changes in the electron density surrounding the atoms in a unit cell. For example, lead titanate ($PbTiO_3$) contains five atoms in the unit cell. This results in $5 \times 3 = 15$ degrees of freedom for the positions of the atomic nuclei in each cell. As these atoms move, the electron density surrounding each atom also evolves. The combined effect of the positive charge of the atomic nuclei and distribution of electron charge density gives a measure of polarization. This can be directly determined with DFT calculations using the Berry phase approach (Resta, 1994). The consequence of using polarization as the order parameter to predict changes in stress and energy during changes in atomic configurations is evaluated for a range of multiaxial strain states.

The phenomenological parameters implemented in the ferroelectric continuum model require computing the energy and stress over a range of polarization values in 3D polarization space (Su and Landis, 2007). Due to complexities that preclude the use of the Cauchy–Born rule to accurately predict atomic displacements in ferroelectric unit cells, a set of calculations about different deformation states is computed to determine the equilibrium atomic positions for different uniaxial and shear deformation states. These results are used as a guide to increment atoms about a fixed strain state which leads to the non-convex energy surface in the polarization space. The DFT code ABINIT is used to calculate the low-energy atomic states for different fixed atomic positions leading to our estimate of the non-convex free energy surface. All energy calculations used in estimating the Landau energy are based on a cubic state as the zero-strain state. The results build upon prior results which estimated a Landau energy function for polarization changes along the direction of spontaneous polarization (Oates, 2014).

The following sections first outline the phenomenological stored energy equations, followed by the DFT calculations and Bayesian statistical analysis. The governing continuum equations are presented in section "Stored energy relations." Within this section, the DFT calculations are summarized giving energy and stress calculations over a range of polarization states. In section "Bayesian uncertainty analysis," Bayesian statistics are used to quantify ferroelectric monodomain parameter uncertainty followed by propagation of errors associated with energy and stress. Numerical results of the model parameters, guided by DFT calculations, are presented in section "Bayesian inference results." In section "Concluding remarks," we provide concluding remarks.

Stored energy relations

The phenomenological stored energy in the ferroelectric solid is divided into elastic, polarization, electrostrictive, and residual energy terms. Since we approximate the internal electronic structure with one electronic coordinate, we assume that a polarization order parameter can be used to accurately represent the solid. In this case, the stored energy per unit volume is $u = u(\boldsymbol{\varepsilon}, \mathbf{P})$, where ε is the total strain and $\mathbf{P}$ is the polarization. The four stored energy density terms considered include

$$u(\boldsymbol{\varepsilon}, \mathbf{P}) = u_M(\boldsymbol{\varepsilon}) + u_P(\mathbf{P}) + u_C(\boldsymbol{\varepsilon}, \mathbf{P}) + u_R(\boldsymbol{\varepsilon}) \tag{1}$$

where u_M is the elastic strain energy, u_P is the Landau energy, u_C is the electrostrictive energy, and u_R is the residual energy due to differences in energy between the cubic and tetragonal states. All energy terms are written per a cubic reference volume. The linear elastic mechanical energy is defined by

$$\begin{aligned} u_M(\varepsilon) = {} & \frac{c_{11}}{2}\left(\varepsilon_{11}^2 + \varepsilon_{22}^2 + \varepsilon_{33}^2\right) \\ & + c_{12}(\varepsilon_{11}\varepsilon_{22} + \varepsilon_{22}\varepsilon_{33} + \varepsilon_{11}\varepsilon_{33}) \\ & + 2c_{44}\left(\varepsilon_{12}^2 + \varepsilon_{23}^2 + \varepsilon_{13}^2\right) \end{aligned} \tag{2}$$

where the elastic components c_{11}, c_{12}, and c_{44} are written using Voigt notation (Malvern, 1969).

Following the notation by (Cao and Cross, 1991), the sixth-order polarization or Landau energy is

$$\begin{aligned} u_P(\mathbf{P}) = {} & \alpha_1\left(P_1^2 + P_2^2 + P_3^2\right) + \alpha_{11}\left(P_1^2 + P_2^2 + P_3^2\right)^2 \\ & + \alpha_{12}\left(P_1^2P_2^2 + P_2^2P_3^2 + P_1^2P_3^2\right) \\ & + \alpha_{111}\left(P_1^6 + P_2^6 + P_3^6\right) \\ & + \alpha_{112}\left[P_1^4\left(P_2^2 + P_3^2\right) + P_2^4\left(P_1^2 + P_3^2\right)\right. \\ & \left. + P_3^4\left(P_1^2 + P_2^2\right)\right] + \alpha_{123}P_1^2P_2^2P_3^2 \end{aligned} \tag{3}$$

where the phenomenological constants are α_1, α_{11}, α_{12}, α_{111}, α_{112}, and α_{123}

The electrostrictive energy is given by

$$\begin{aligned} u_C(\boldsymbol{\varepsilon}, \mathbf{P}) = & -q_{11}\left(\varepsilon_{11}P_1^2 + \varepsilon_{22}P_2^2 + \varepsilon_{33}P_3^2\right) \\ & -q_{12}\left[\varepsilon_{11}\left(P_2^2 + P_3^2\right)\right. \\ & \left. + \varepsilon_{22}\left(P_1^2 + P_3^2\right) + \varepsilon_{33}\left(P_1^2 + P_2^2\right)\right] \\ & -4q_{44}(\varepsilon_{12}P_1P_2 + \varepsilon_{13}P_1P_3 + \varepsilon_{23}P_2P_3) \end{aligned} \tag{4}$$

where q_{11}, q_{12}, and q_{44} are the electrostrictive coefficients.

The DFT analysis described in the following section focuses on energy, stress, and polarization computations. The polarization is treated as the model input to the continuum model, and the continuum model outputs of energy and stress are compared to DFT energy and stress calculations. This requires careful assessment of atomic motion to prescribe a specified polarization at fixed strain as discussed in the following section. Importantly, we hold the unit cell fixed so that the total strain is defined to be zero in a prescribed cubic state. This produces a residual energy term that we define in terms of a residual stress tensor. This residual energy is

$$u_R = \sigma_{ij}^R \varepsilon_{ij} \tag{5}$$

where σ_{ij}^R is the unknown residual stress required to constrain the unit cell to the cubic state. This stress tensor will be treated as a random parameter and determined from DFT computations through the use of Bayesian statistics.

The effect of electrostriction and residual stress is evaluated by comparing continuum stress using the definition

$$\sigma_{ij} = \frac{\partial u}{\partial \varepsilon_{ij}} \tag{6}$$

which leads to elastic, electrostrictive, and residual stresses. For example, consider the general tensor forms of the elastic and electrostrictive coefficients using $c_{ijk\ell}$ and $q_{ijk\ell}$, respectively. The stress tensor is then

$$\sigma_{ij} = c_{ijk\ell}\varepsilon_{k\ell} - q_{ijk\ell}P_kP_\ell + \sigma_{ij}^R \tag{7}$$

Using the cubic reference state as the zero-strain state ($\varepsilon_{ij} = 0$), we can quantify the spontaneous strain in terms of polarization and a residual stress at zero polarization. To obtain the spontaneous strain, the total stress is set to zero and the total strain from equation (7) is

$$\varepsilon_{ij} = s_{ijkl}q_{klrs}P_rP_s - s_{ijkl}\sigma_{kl}^R \tag{8}$$

where s_{ijkl} is the compliance tensor (Malvern, 1969). Under this relaxed condition of zero stress, the two strain components include polarization-induced strain and strain from residual stress at zero polarization. Using conventional notation (Völker et al., 2011), we define the spontaneous strain as a function of polarization. In particular, the spontaneous strain is defined at the minimum total energy at zero stress. We define the spontaneous polarization state ($P_r \rightarrow P_r^S$) under these conditions which gives the spontaneous strain, $\varepsilon_{ij}^S = s_{ijkl}q_{klrs}P_r^SP_s^S$. The remaining term in equation (8) is defined as the residual strain at zero polarization, $\varepsilon_{ij}^R = -s_{ijkl}\sigma_{kl}^R$.

In the numerical analysis, we focus on identifying phenomenological parameters excluding the elastic coefficients. Since the elasticity has been studied extensively, we neglect quantifying this uncertainty and instead assume fixed elastic properties from previous DFT calculations (King-Smith and Vanderbilt, 1994). As will be discussed in section "Bayesian uncertainty analysis," it was determined that the values of elastic properties are sensitive in obtaining a convex energy landscape under zero-stress conditions.

DFT calculations

We conducted a set of DFT calculations using ABINIT to determine energy and stress for different uniform polarization states such that the continuum-scale Landau energy and electrostrictive stresses could be quantified. Prior one-dimensional (1D) results described by Oates (2014) for lead titanate are combined with energy calculations that estimate the stored energy for a broader range of polarization states that can be used to determine equation (3) for two-dimensional (2D) and 3D problems. Additional calculations of stress allow us to determine equation (4). Pseudopotentials developed previously within this code were used to approximate the electron density. All DFT simulations used a $10 \times 10 \times 10$ k-point grid on a five-atom lead titanate unit cell with a cut-off energy of 60 Ha (1633 eV). The local density approximation (LDA) was also used in all calculations.

Prior DFT results were calculated by first identifying equilibrium atomic positions in the fully relaxed equilibrium lattice configuration in the tetragonal state. The atoms were then incremented in the cubic state with lattice dimensions $a \times a \times a = 57.4\,\text{Å}^3$ starting with the centrosymmetric atomic configuration and linearly incrementing the atoms through the equilibrium tetragonal state. This yields a double-well potential energy function.

This double-well potential is estimated using the following methodology. In general, the atomic position degrees of freedom are described by the vector Π_i^a for each of the five atoms ($a = Pb$, Ti, $2 \times O_\parallel$, and $O_\perp$) in the unit cell. The atom labels and the atomic displacements for the titanium atom (as an example) are illustrated in Figure 1.

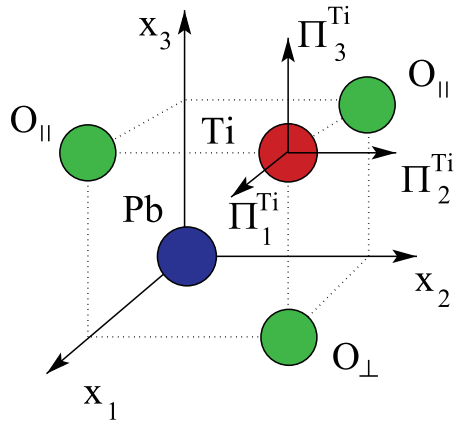

Figure 1. Description of the atoms contained within the lead titanate unit cell. An example of the atomic displacements (Π_i^a) is shown for the titanium atom.

As described previously (Oates, 2014), the displacements along the x_3 direction are related to a single atomic displacement order parameter. The component of this order parameter, denoted by Π_3, defines the displacements of each atom along x_3 according to

$$\begin{aligned} \Pi_3^{O_\perp} &= \alpha\Pi_3 \\ \Pi_3^{Pb} &= \beta\Pi_3 \\ \Pi_3^{O_\parallel} &= \gamma\Pi_3 + \mu \\ \Pi_3^{Ti} &= \nu\Pi_3 + \mu \end{aligned} \tag{9}$$

where the constants α, β, γ, ν, and μ are given in Oates (2014). This relationship maps a single atomic displacement Π_3 along the x_3 direction to the positions of each of the five atoms.

To quantify a stored energy surface for polarization states not aligned with the spontaneous polarization direction, atomic displacements under internal atomic shearing are used to estimate the energy surface for a broader range of polarization states. Due to crystal symmetry of lead titanate, this requires incrementing the polarization by an angle ranging from 0° to 45° for different polarization magnitudes. We estimate the motion of the atoms that is expected to occur during polarization reorientation starting from full alignment in the x_3 direction to 45° rotation toward the x_2 direction. This allows the identification of all Landau parameters in equation (3) except α_{123}.

Continuum parameter identification is done by conducting a series of *ab initio* molecular dynamic simulations about several fixed unit cell shear deformation states and simultaneously determining the equilibrium atomic positions and electron density. Entropic effects are neglected by computing energy, stress, and polarization in the limit of 0 K. The minimization method used in the molecular dynamic simulations is based on the Broyden–Fletcher–Goldfard–Shanno method contained within ABINIT 7.0.5 (Gonze et al., 2009). The deformation gradient component $F_{23} = \partial x_2/\partial X_3$, based on conventional deformation notation (Malvern, 1969), is incremented from 0 up to 0.17 while holding all other deformation gradient components fixed. Once these equilibrium configurations are determined, the polarization is determined using the Berry phase approach (Resta, 1994). This approach is used to relate polarization to atomic positions to quantify the Landau energy in the fixed strain state. An example of the differences in atomic and electronic structures in the undeformed reference state and shear-deformed state is shown in Figure 2.

To induce a P_2 polarization component, we assume that the five atoms within the unit cell move proportional to their Π_3^a positions. This is described by

$$\Pi_2^a = \Pi_2^{j,a} + \chi\Pi_3^{j,a} \tag{10}$$

where $\Pi_2^{j,a}$ and $\Pi_3^{j,a}$ constitute the nominal atomic positions for spontaneous polarization aligned in the P_3 direction. The constant χ scales the Π_2^a displacements by a fraction of the respective Π_3^a displacements. Note that $j = 1, \ldots, N$ includes 13 points of DFT computations along the P_3 space with $P_2 = 0$. We conduct DFT simulations along five thermodynamic paths in shear.

The linear approximation of the atom positions with respect to the different F_{23} values is shown in Figure 3(a) for the titanium atom position in the $x_2 - x_3$ plane. Figure 3(b) illustrates how the polarization changes as the titanium atom displaces in shear. All atoms have similar characteristics which we approximate to follow the relation in equation (10) when estimating the stored energy and stress during polarization rotation, $P_3 \rightarrow P_2$.

The changes in stored energy as a function of atomic displacements are computed using DFT calculations while holding the unit cell fixed at a reference cubic state using the same unit cell geometry as prior uniaxial results (Oates, 2014). This simplifies combining prior energy calculations with the new calculations given here; however, it introduces uncertainty between the position of the atoms and the resulting polarization when using the cubic state as the reference configuration as shown in Figure 3(b). The thermodynamic path during shear deformation may follow a more complex atomic displacement trajectory; however, we show reasonable estimates of continuum-scale energy and stress along these paths. The error propagation afforded by Bayesian statistics highlights varying degrees of uncertainty as feedback for model refinement.

Using the relationship defined by equation (10), the atoms were linearly incremented from different atomic positions starting near the centrosymmetric state through the equilibrium tetragonal state. The five paths defining polarization rotation ($P_3 \rightarrow P_2$) are shown in Figure 4. For these five starting points where $P_2 = 0$,

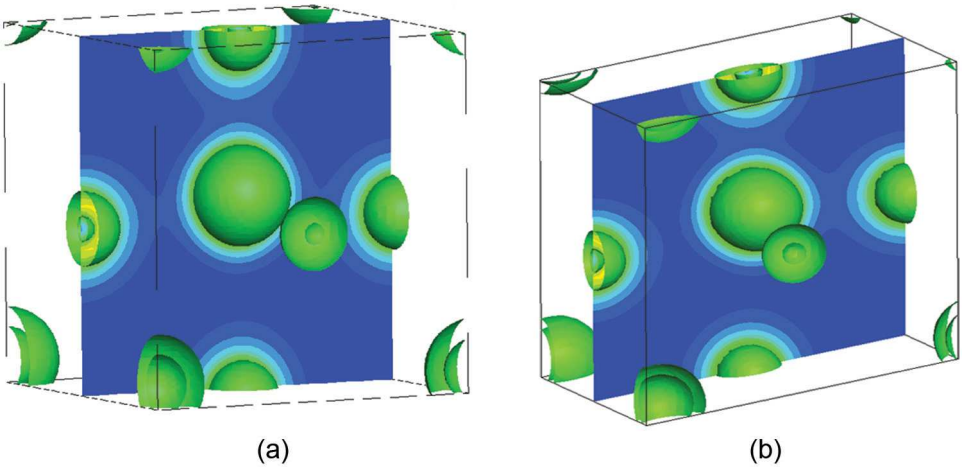

Figure 2. Example of the electron density solutions for (a) the reference undeformed cubic structure and (b) shear-deformed state where the unit cell has been sheared such that the deformation gradient component F_{23} is non-zero.

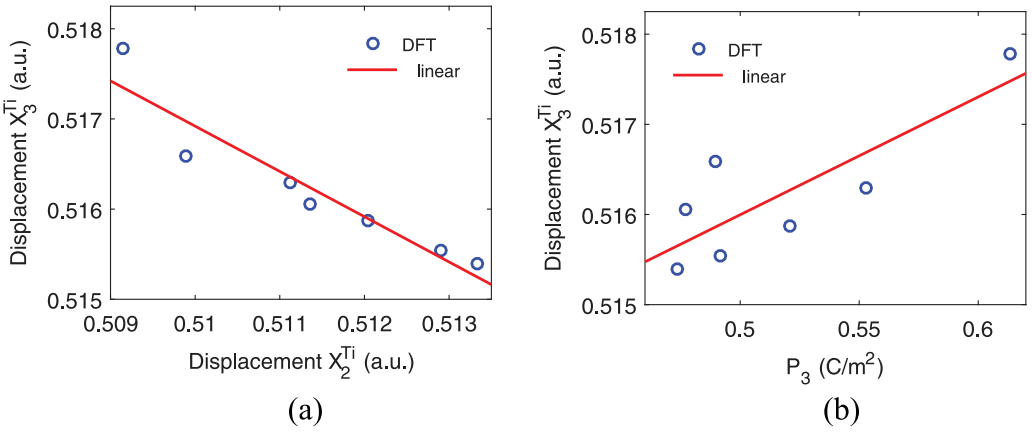

Figure 3. (a) Atomic displacement showing the relationship between the position of the titanium atom in the x_2 and x_3 directions as the deformation component F_{23} varies between 0 and 0.17. (b) Relationship between the atomic position (titanium atom) and polarization in the x_3 direction as the deformation gradient component F_{23} varies between 0 and 0.17.

the atoms are moved along the directions estimated from the shear deformation (F_{23}) simulations to generate positive P_2 values while P_3 is reduced. Again note that all the results in Figure 4 are obtained under a constrained cubic state. Berry phase polarization was calculated along with the total energy which can be seen in Figure 4(a). The stress tensor was also calculated and the shear stress component σ_{23} is shown as a function of polarization in Figure 4(b). The results illustrate how displacements of the atoms lead to polarization rotation, giving rise to changes in energy and shear stress over a polarization rotation of approximately 45°. We will show in the following section how Bayesian statistics can be used to estimate the continuum electrostrictive and Landau parameters and the uncertainty associated with calibrating the ferroelectric continuum model in light of these DFT calculations.

Bayesian uncertainty analysis

Bayesian statistics assert that the model parameters contain uncertainty when calibrated to experimental measurements or higher fidelity models. Here, the DFT calculations are considered the higher fidelity results and the homogenized continuum parameters are calibrated to these results based on the parameters outlined in section "Stored energy relations." To accommodate uncertainty in Bayesian inference, parameters are taken to be random variables having associated probability density functions (PDFs) or distributions. Details regarding this approach are provided in Chapter 8 of Smith (2013). The continuum model calibration to DFT simulations focuses on parameter uncertainty of a monodomain structure. The Landau parameters contained within the stored energy density (equation (3)) and the electrostrictive parameters contained within the electromechanical energy density in equation (4) are

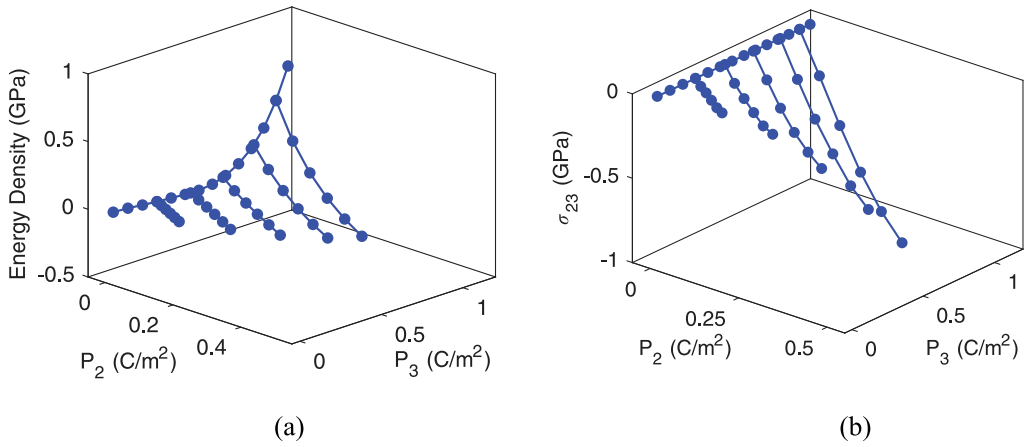

Figure 4. (a) Total energy and (b) shear stress (σ_{23}) as a function of P_2 and P_3.

quantified first. These parameters are determined from the DFT energy, stress, and polarization calculations summarized in section "Stored energy relations." Through this analysis, we discuss how the identification of Landau and electrostrictive parameters can be decoupled and inferred separately.

The sets of phenomenological constants identified from the monodomain Bayesian statistics are denoted by θ_P and θ_σ, which correspond to parameters for the Landau energy density and electrostrictive stresses, respectively. These parameters are

$$\begin{aligned}\theta_P &= [\alpha_1, \alpha_{11}, \alpha_{12}, \alpha_{111}, \alpha_{112}] \\ \theta_\sigma &= \left[q_{11}, q_{12}, q_{44}, \sigma^R_{11}, \sigma^R_{22}, \sigma^R_{33}, \sigma^R_{23}\right]\end{aligned} \tag{11}$$

The parameters contained in each set can be inferred separately due to the independence between the strain and polarization in the Landau and electrostictive energy densities. In the case of θ_P, we compare the total DFT energy to the continuum Landau energy density. The electrostrictive and residual energies are zero in this case since the strain is set to zero in the reference cubic state. The parameters within θ_σ are determined by comparing DFT stress to continuum-scale stresses. Also note that the stress components in θ_σ represent residual stress due to the reference configuration chosen for the DFT simulations. Since the polarization is constrained to move from the P_3 to P_2 direction, we take advantage of symmetry where $\sigma^R_{11} = \sigma^R_{22}$ and $\sigma^R_{12} = \sigma^R_{13} = 0$. This was confirmed through DFT simulations and also verified using Bayesian statistics by allowing continuum estimates of σ^R_{11} and σ^R_{22} to be independent. We leave σ^R_{23} in the calculations although its mean estimate is found to be approximately zero. Despite a zero-mean residual shear stress, the uncertainty in its value can contribute to uncertainty in the total stress which will be indicated through propagation of errors. We can decouple the analysis of normal and shear stresses, thereby allowing us to analyze the parameter sets

$$\theta_{\sigma_{ns}} = \left[q_{11}, q_{12}, \sigma^R_{11}, \sigma^R_{22}, \sigma^R_{33}\right],\ \theta_{\sigma_s} = \left[q_{44}, \sigma^R_{23}\right] \tag{12}$$

separately. The analysis is performed in both ways to highlight how the uncertainty propagates through all the model parameters.

A statistical model is introduced which incorporates the physical model with random errors associated with aleatoric uncertainty between DFT calculations of stress and energy and the corresponding continuum approximation. The statistical model is taken to be

$$M^{DFT}(s) = M(s;\theta) + \varepsilon_s, \quad s = 1, \ldots, n \tag{13}$$

where DFT calculations are denoted by $M^{DFT}(s)$ and ε_s are the errors induced by the continuum model $M(s;\theta)$. All errors are assumed to be independent and identically distributed (iid). The DFT (M^{DFT}) and continuum ($M(s;\theta)$) models may include measures of monodomain energy and electrostrictive stress. Each model will be specified and compared to continuum estimates in the following sections.

Bayesian model calibration utilizes Bayes' equation

$$\pi\left(\theta_k | M^{DFT}\right) = \frac{\ell(M|\theta_k)\pi_0(\theta_k)}{\int\limits_{\mathbb{R}^s} \ell(M|\theta_k)\pi_0(\theta_k)d\theta_k} \tag{14}$$

to infer the probability densities of the continuum parameters based on DFT calculations. In equation (14), the continuum model output denoted by M describes the monodomain material characteristics, while θ_k denotes the model parameters in equation (11). The posterior density, $\pi(\theta_k|M^{DFT})$, quantifies the probability of observing the parameter values θ_k given the DFT energy or stress calculations which is denoted by M^{DFT}. The prior density is denoted by $\pi_0(\theta_k)$, which assumes previous knowledge about the model parameters before comparing to the DFT calculations. We assume flat priors for all parameters unless otherwise noted. These priors are characterized as having a constant value on a parameter space that satisfies positive definite

thermodynamic criteria. The prior densities are updated using a likelihood $\ell(M|\theta_k)$, which compares the model outputs given by the continuum model and the DFT model. The denominator in Bayes' equation normalizes the posterior density to have an area of unity.

The likelihood function used here assumes that errors in the DFT energy and stress calculations are iid and normally distributed with zero mean and variance σ_k^2, $\varepsilon_k \sim N(0, \sigma_k^2)$. The likelihood function is then

$$\ell(M|\theta_k) = e^{-\sum_{s=1}^{N} \frac{[M^{DFT}(s) - M(s;\theta_k)]^2}{2\sigma_k^2}} \tag{15}$$

which assumes that the DFT energy and stress calculations are normally distributed as $M^{DFT}(s) \sim N(M(s;\theta_k), \sigma_k^2)$. In this equation, we have explicitly included the number of model outputs evaluated over $s = 1, \ldots, N$. The variance σ_k in the DFT calculations is unknown and is inferred during the calibration of the continuum model parameters θ_k. We presume that this variance may be different for the DFT energy and stress calculations.

There are five unknown parameters in θ_P and seven parameters in θ_σ that are all numerically inferred through the Bayesian calibration. Whereas the parameter sets are reasonably small, Gauss quadrature techniques are not ideal due to the order of integration in the denominator contained within equation (14) and also due to the lack of a priori knowledge of the limits of integration. These computational issues are avoided by implementing sampling-based Metropolis algorithms, the stationary distribution of which is the posterior density. In particular, the delayed rejection adaptive Metropolis (DRAM) algorithm developed by Haario et al. (2001, 2006) is implemented using the code available on the website (Laine, 2013).

Bayesian inference results

Here we summarize the results from the Bayesian statistical analysis of the Landau energy and monodomain stresses. We highlight parameter uncertainty in both Landau energy and electrostrictive parameters and how this uncertainty propagates through the continuum model when predicting continuum-scale energy and stress as a function of polarization.

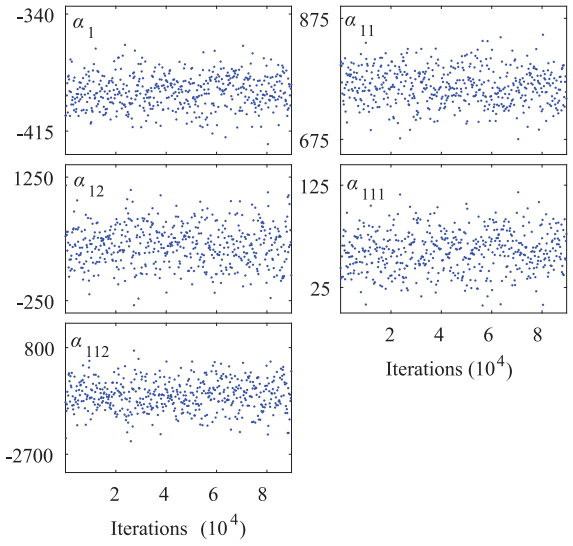

Figure 5. Statistical sampling results for the Landau energy model parameters in the continuum model using DFT energy calculations. 1×10^5 iterations were used in the simulations.

Model calibration: monodomain energy

The continuum model calibration is conducted by sampling over the monodomain DFT energy and stress calculations presented in section "Stored energy relations." The number of model iterations was 1×10^5 for all analyses. A summary of the mean values and standard deviations for the Landau parameters is given in Table 1. Both sixth- and fourth-order models—$\alpha_{111} = \alpha_{112} = 0$ in equation (3)—are evaluated for comparisons of the energy landscapes given in the subsequent discussion in section "Bayesian inference results." The results of the energy calibration illustrate important differences in the amount of relative

Table 1. Landau energy parameters determined using Bayesian statistics implemented via DRAM.

Symbol	Mean value (6th order)	Standard deviation	Units
α_1	−389.4	10.49	MV m/C
α_{11}	761.3	30.01	MV m^5/C^3
α_{12}	414.1	241.6	MV m^5/C^3
α_{111}	61.46	19.98	MV m^9/C^5
α_{112}	−740.8	499.4	MV m^9/C^5
Symbol	Mean value (4th order)	Standard deviation	Units
α_1	−414.1	5.925	MV m/C
α_{11}	846.4	6.904	MV m^5/C^3
α_{12}	−80.73	57.22	MV m^5/C^3

DRAM: delayed rejection adaptive Metropolis.

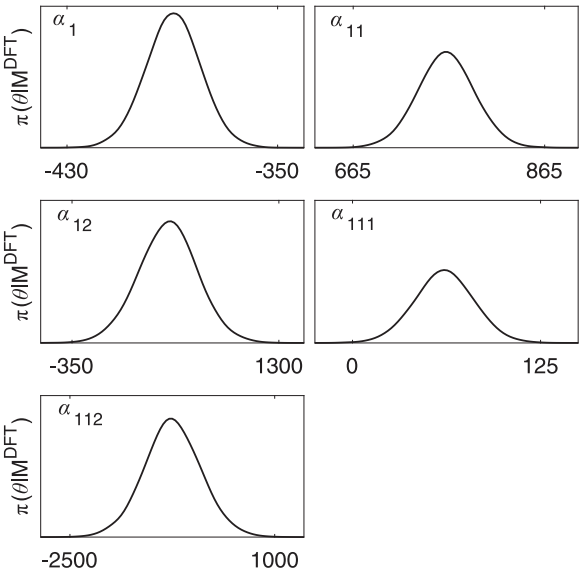

Figure 6. Bayesian marginal posterior densities ($\pi(\theta|y^{DFT})$) for the continuum model parameters.

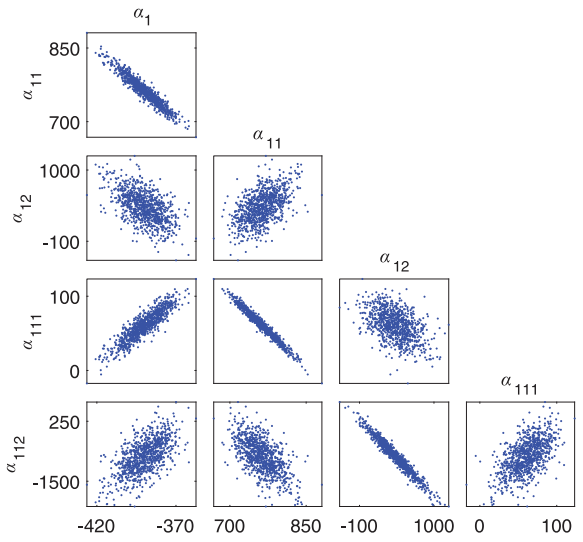

Figure 7. Pairwise correlation among the Landau energy parameters. Stronger correlation is observed between some of the lower and higher order parameters.

uncertainty for each parameter by comparisons of mean values and their standard deviations. For example, the second- and fourth-order Landau parameters α_1 and α_{11} have lower relative uncertainty in comparison to α_{12} and the sixth-order terms.

Statistical results based on the Landau energy density in Figures 5 and 6 show the parameter samples generated using the DRAM algorithm and the resulting posterior densities, respectively. The parameters sampled for 1×10^5 iterations in Figure 5 illustrate a "burned-in" chain among all the Landau model parameters considered. A burned-in chain is defined by a chain that has been sampled sufficiently such that it has converged to the posterior density. The posterior probabilities for the Landau energy density parameters are determined from these chains. All the posterior probabilities are approximately normal distributions as shown in Figure 6. Correlation between certain parameters is also quantified as shown in Figure 7. Stronger correlation is seen among (α_1, α_{11}), $(\alpha_{11}, \alpha_{111})$, and $(\alpha_{12}, \alpha_{112})$. The simplest example of parameter correlation is the inverse relation between α_1 and α_{11} as these parameters govern the polarization at minimum energy which is $P_0 = \sqrt{-\alpha_1/2\alpha_{11}}$, where electrostriction and the sixth-order terms are neglected. A similar competing mechanism for P_0 occurs between the higher order α_{111} term and α_{11} as shown by their correlation in Figure 7. Finally, the α_{12} and α_{112} parameters are associated with polarization rotation, which is supported by their correlation.

We also quantify the uncertainty in the model output by propagating the errors through the Landau energy function based on the combination of the posterior densities in Figure 6 and the inferred variance σ_k^2 from equation (15). This provides measures of the mean Landau energy as well as credible and prediction intervals relative to the DFT energy; details on these intervals in comparison to frequentist-based confidence intervals are described in Smith (2013). The Landau energy density using mean parameter values versus the DFT energy density are shown in Figure 8(a) for the full sixth-order polynomial energy representation. We also compare the fourth-order Landau model to the sixth-order model fit. The comparison of the fourth- and sixth-order models is illustrated by plotting the residual error between the continuum energy and the DFT energy in Figure 8(b). The results show comparable residual errors for the fourth- or sixth-order models; however, there are important differences that will be discussed at the end of this section. We first identify the electrostrictive parameters and then combine these parameters into a measure of the total energy to assess the different polynomial orders of the Landau energy.

The 95% prediction and credible intervals shown in Figure 8(a) are further highlighted by plotting the error propagation of the Landau energy along select thermodynamic paths. The prediction and credible intervals are relatively small overall; therefore, 95% intervals along two different lines of polarization are shown in Figure 9 to highlight their differences. The plot in Figure 9(a) corresponds to line 1 in Figure 8(a) where $P_2 = 0$, and the plot in Figure 9(b) corresponds to line 4 among the five lines from Figure 8(a) where $P_2 \neq 0$. The prediction and credible intervals appear larger along the lines where $P_2 \neq 0$ because the magnitude of the energy is smaller and the uncertainty on α_{12} and α_{112} is larger than on the other Landau parameters.

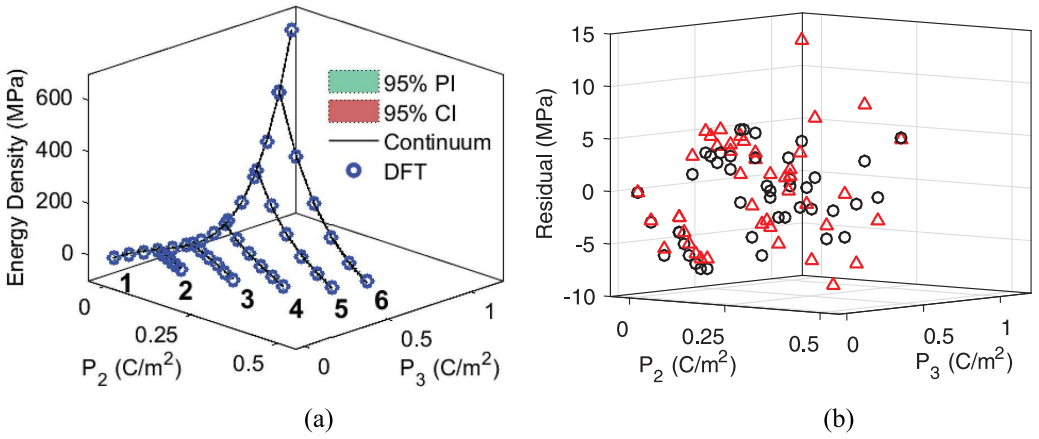

Figure 8. (a) Continuum model comparison of the sixth-order Landau energy in comparison to the DFT energy function including 95% prediction and credible intervals. Note that each line consists of a set of energy values along different lines in the P_2P_3-plane. The lines have been numbered 1–6 for reference in later discussion. (b) A scatter plot of the error using the full sixth-order Landau energy function in equation (3) (black circles) versus a lower order fourth-order Landau energy function (red triangles).

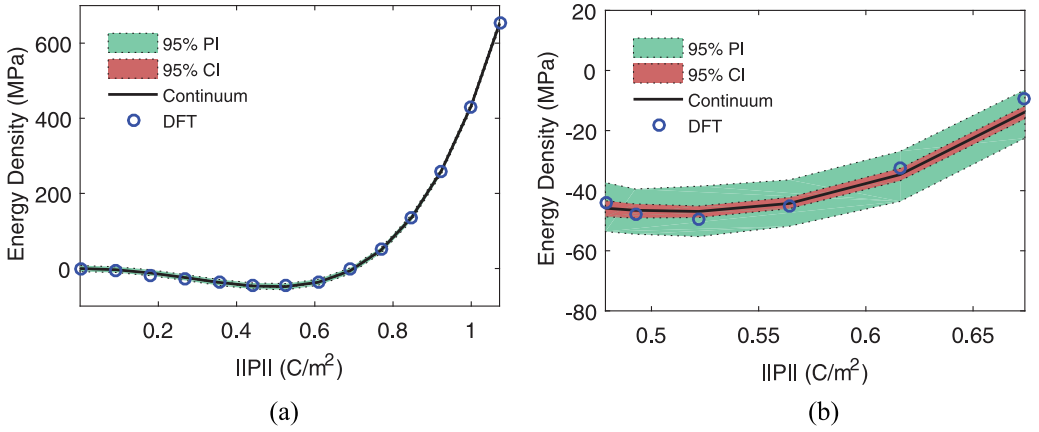

Figure 9. Error propagation of the energy function, u_P, about two different lines along the stored energy path plotted against the polarization magnitude $||P||$: (a) energy for line 1 in Figure 8(a) for the case where $P_2 = 0$ and (b) energy for line 4 in Figure 8(a) for the case where $P_2 \neq 0$.

Table 2. Continuum material parameters determined using Bayesian statistics via DRAM. Parameters with an asterisk were inferred using θ_{σ_s}.

Symbol	Mean value	Standard deviation	Units
q_{11}	19.2	0.258	GV m/C
q_{12}	3.14	0.182	GV m/C
q_{44}	1.39	0.538	GV m/C
q_{44}^*	1.40	0.019	GV m/C
σ_{11}^R	−3.977	0.103	GPa
σ_{22}^R	−3.995	0.101	GPa
σ_{33}^R	−3.410	0.118	GPa
σ_{23}^R	-4.00×10^{-4}	96.2×10^{-3}	GPa
σ_{23}^{R*}	-7.79×10^{-4}	3.32×10^{-3}	GPa

DRAM: delayed rejection adaptive Metropolis.

These two parameters do not influence the energy when $P_2 = 0$.

Model calibration: monodomain stresses

A similar set of Bayesian statistical results are calculated for the electrostrictive stress constitutive law given by equation (4) in light of the DFT stress calculations. The electrostrictive coefficients and residual stress components contained within θ_σ are summarized in Table 2. Again 1×10^5 iterations are calculated to ensure that the parameter values are burned-in similar to the results shown in Figure 5. For brevity, we only show statistical results in terms of the posterior densities of the electrostrictive parameters and the residual stress. The results are in agreement with the means and standard deviations given in Table 2 which show larger uncertainty in the shear coefficient q_{44} when it is identified together with all parameters in θ_σ. When θ_{σ_s} is identified, the standard deviation of the shear parameters is significantly reduced. Also note that the shear

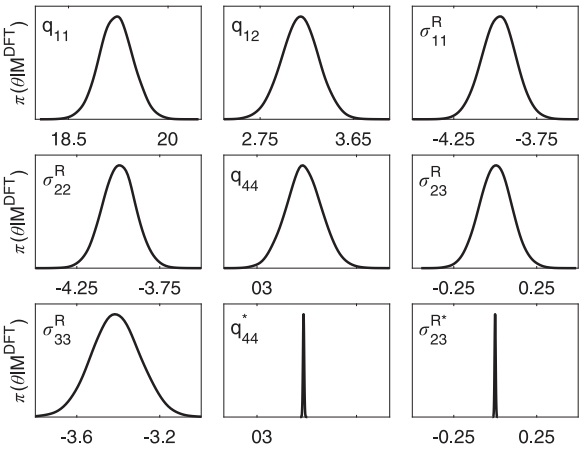

Figure 10. Bayesian marginal posterior densities ($\pi(\theta|y^{DFT})$) for the electrostrictive parameters and residual stress in the continuum model. The units for the parameter values are given in Table 2. By decoupling the model, it is seen that the uncertainty in the shear stress parameters (q_{44} and σ^R_{23}) has been reduced. Note that these shear stress parameters are normally distributed, but the view is expanded to highlight the decrease in uncertainty.

residual stress is nominally zero as expected; however, there is uncertainty associated with its value. The posterior densities for both θ_σ and θ_{σ_s} are shown in Figure 10. All posteriors are approximately normal distributions. Importantly, we find reduced uncertainty when the shear parameters are identified independently from the normal stress parameters. The uncertainty of the normal stress parameters is unaffected by decoupling the parameter estimation.

It is important to refer back to equation (4) to highlight the decoupling between the electrostrictive parameters q_{11} and q_{12} associated with normal stress and the shear electrostrictive coefficient q_{44}. Upon simplifying the stress from equation (7), it can be shown that the electrostrictive shear stress depends only on the uncertain parameters q_{44} and σ^R_{23}. Therefore, these parameters may be sampled separately from the normal stress components to determine how this influences parameter identification and uncertainty. In the following, we compare sampling all stress parameters contained within θ_σ versus the reduced set defined by $\theta_{\sigma_s} = [q_{44}, \sigma^R_{23}]$.

The mean model predictions of the relevant stress components along with their prediction and credible intervals are shown in Figure 11 using the parameter set θ_σ. Similar to the case of the Landau energy surface, reasonable predictions are observed over the range of polarization values simulated; however, the range of uncertainty in electrostrictive stress is more difficult to see over the entire polarization space. Selected 1D plot examples examining σ_{33} and σ_{23} are shown in Figures 12 and 13, respectively, to further illustrate the propagation of uncertainty. Note that the error propagation in Figure 13 is based on the reduced uncertainty using parameters θ_{σ_s}. It is clearly shown that less uncertainty exists for the normal stress along the direction of polarization when $P_2 = 0$; similar results are found for σ_{11} and σ_{22}. The shear stress and normal stresses for the cases where $P_2 \neq 0$ exhibit larger uncertainty. This is due to the magnitude of the stress, the larger uncertainty in the shear electrostrictive parameter q_{44}, and the additional uncertainty of the shear residual stress. However, as mentioned earlier, by decoupling the parameter identification between the normal and shear stresses, there is a significant decrease in the uncertainty contained within the shear electrostrictive and shear residual stress parameters.

Model comparison at zero-strain and zero-stress states

Given the parameter calibration for both the Landau energy and electrostrictive stresses, we further analyze the energy landscape under zero-strain and zero-stress states. The total energy under zero strain is fully described by the Landau energy. This form of the energy is compared to the total energy where the stress is set to zero. We set the stress to zero and solve for the spontaneous strain in terms of polarization to find this form of the total energy. These strain components are substituted into u_M from equation (2) and u_C from equation (4) to obtain the total stored energy in terms of polarization. In this comparison, we set the residual stresses to zero in the residual energy from equation (5) since it produces biased minimum wells along the P_3 polarization direction. In this case, the elastic, electrostrictive, and Landau energies are all non-zero and plotted together, for example, $u_{Tot}(P_i) = u_P(P_i) + u_M(P_i) + u_C(P_i)$. This relaxed state is compared to the Landau energy under zero strain as shown in Figure 14. In all plots, we apply mean parameter values.

It is particularly interesting to compare the zero-strain and zero-stress total energies using the sixth- versus fourth-order Landau energy densities. The fourth-order Landau energy Bayesian calibration results in a non-negligible increase in error. The error, based on the mean parameter estimates and using a sum of squares difference between the Landau and the DFT energies, increases from 24.7 MPa for the sixth-order model to 32.3 MPa for the fourth-order model. The pointwise differences in the residual errors, as shown in Figure 8(b), are small relative to the maximum energy (650 MPa). However, it becomes significant when compared to the energy at zero polarization versus the energy minimum, that is, $\Delta u = 46.3$ MPa. These differences are most apparent by comparing the energy landscapes of the sixth- and fourth-order models in Figure 14(a) and (c), respectively. The fourth-order model predicts a rhombohedral phase, while the sixth-order

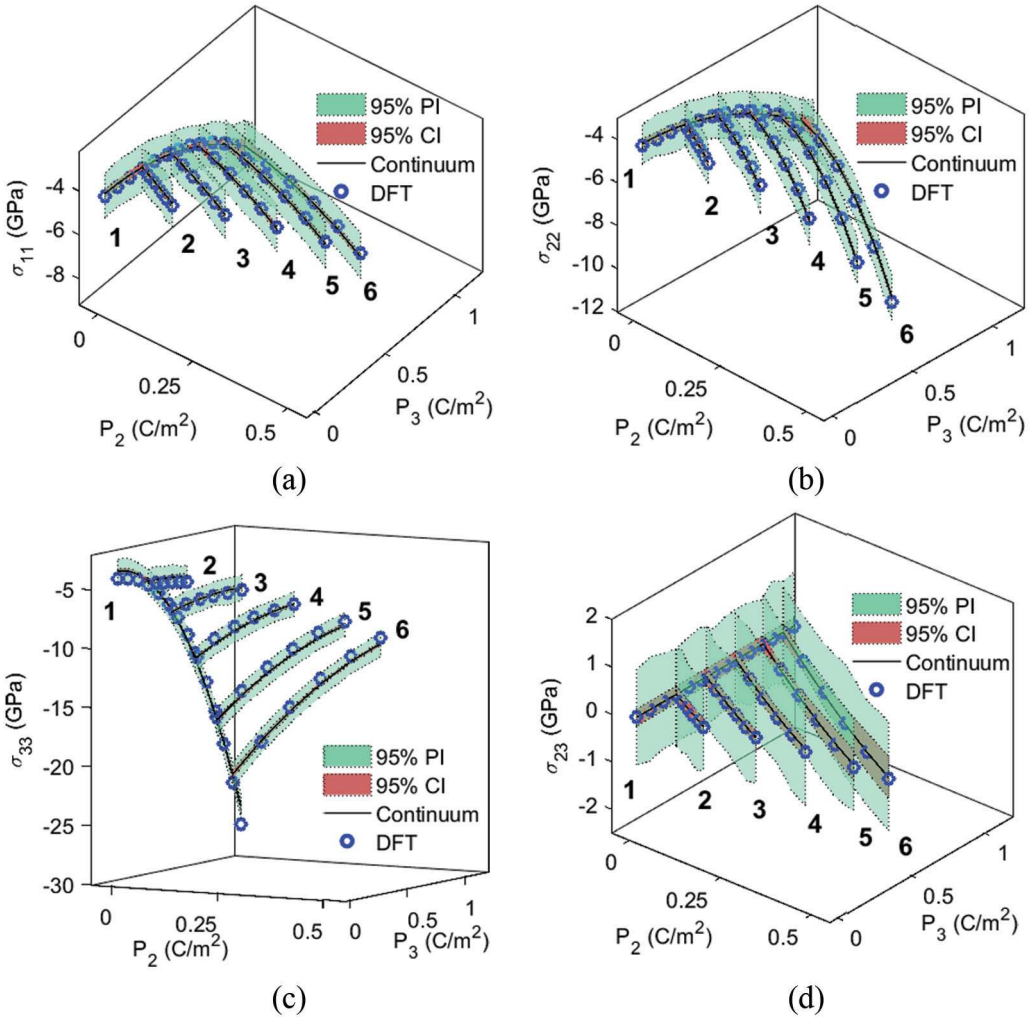

Figure 11. Examples of the mean model estimates along with 95% prediction (PI) and credible (CI) intervals in relation to DFT stresses for (a) σ_{11}, (b) σ_{22}, (c) σ_{33}, and (d) σ_{23}. Note that each plot consists of a set of stresses along different lines in the P_2P_3-plane. The lines have been numbered 1–6 for reference in later discussion.

model predicts a tetragonal phase for the zero-strain state. The differences in these two approximations is primarily attributed to α_{12} which changes its sign when using a fourth- or sixth-order polynomial as given in Table 1. In contrast, α_1 and α_{11} are insensitive to the order of the model calibration. The minima directions predicted by the fourth-order model are self-consistent with prior DFT analysis on lead titanate (King-Smith and Vanderbilt, 1994).

Figure 14(b) and (d) represents the sixth- and fourth-order energy densities, respectively, for the zero-stress state. In these plots, we use the mean electrostrictive parameters from Table 2 in combination with elastic moduli from King-Smith and Vanderbilt (1994). For reference, the elastic properties used in the model include $c_{11} = 321\,\text{GPa}$, $c_{12} = 140\,\text{GPa}$, and $c_{44} = 96.5\,\text{GPa}$. In both the sixth- and fourth-order models, the magnitudes of polarization at the minima have increased due to relaxation as expected. In addition, the location of the minima in the fourth-order model has reoriented from the rhombohedral direction to the tetragonal direction, consistent with experimental observation and DFT calculations (Jaffe, 2012; King-Smith and Vanderbilt, 1994; Shirane et al., 1956). It is also important to note how the continuum energy landscape is sensitive to both the electrostrictive and elastic coefficients. For example, if the elastic modulus was taken to be smaller (e.g. elastic tensor values from lead titanate thin films (Ruglovsky et al., 2006)), the total energy density in the relaxed state becomes convex and grows unbounded in the negative direction as the polarization increases.

It was highlighted in Table 1 that the sixth-order terms have higher relative uncertainty than the fourth-order terms. This is expected since the DFT calculations were taken for polarization values less than or near the spontaneous polarization. These sixth-order terms become more sensitive at larger polarization

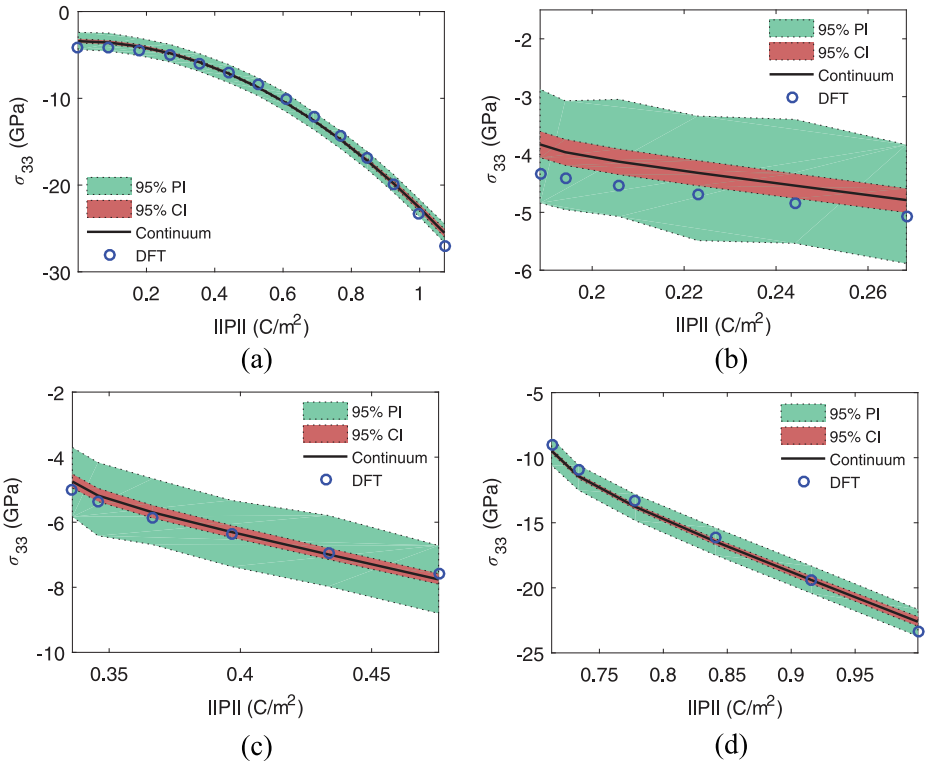

Figure 12. Error propagation for σ_{33} with respect to the magnitude of polarization. The plots reflect 2D representations of the error propagation shown in Figure 11(a): (a) line 1, (b) line 2, (c) line 3, and (d) line 6. Note that 95% prediction intervals (PIs) and credible intervals (CIs) are shown in relation to the σ_{33} stress.

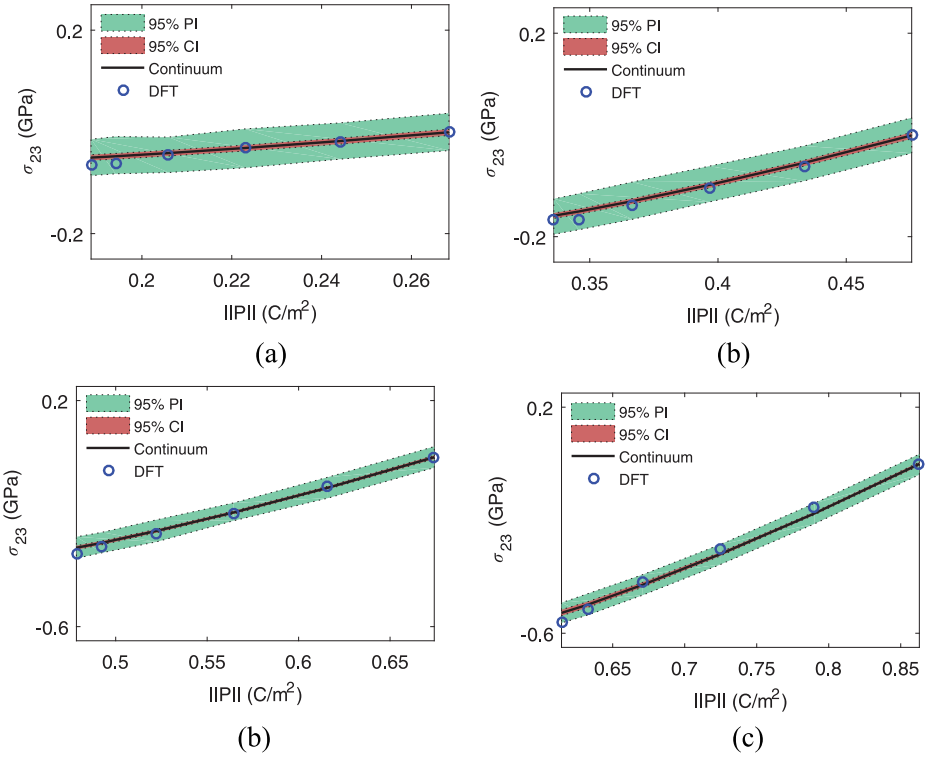

Figure 13. Error propagation for σ_{23} with respect to the magnitude of polarization. Results shown of calibration using $\theta_{\sigma 2}$. In reference to Figure 11(d), (a) line 2, (b) line 3, (c) line 4, and (d) line 5. Note that 95% prediction intervals (PIs) and credible intervals (CIs) are shown in relation to the σ_{23} stress. It is clearly seen that the prediction and credible intervals are significantly decreased compared to those observed in Figure 11(d).

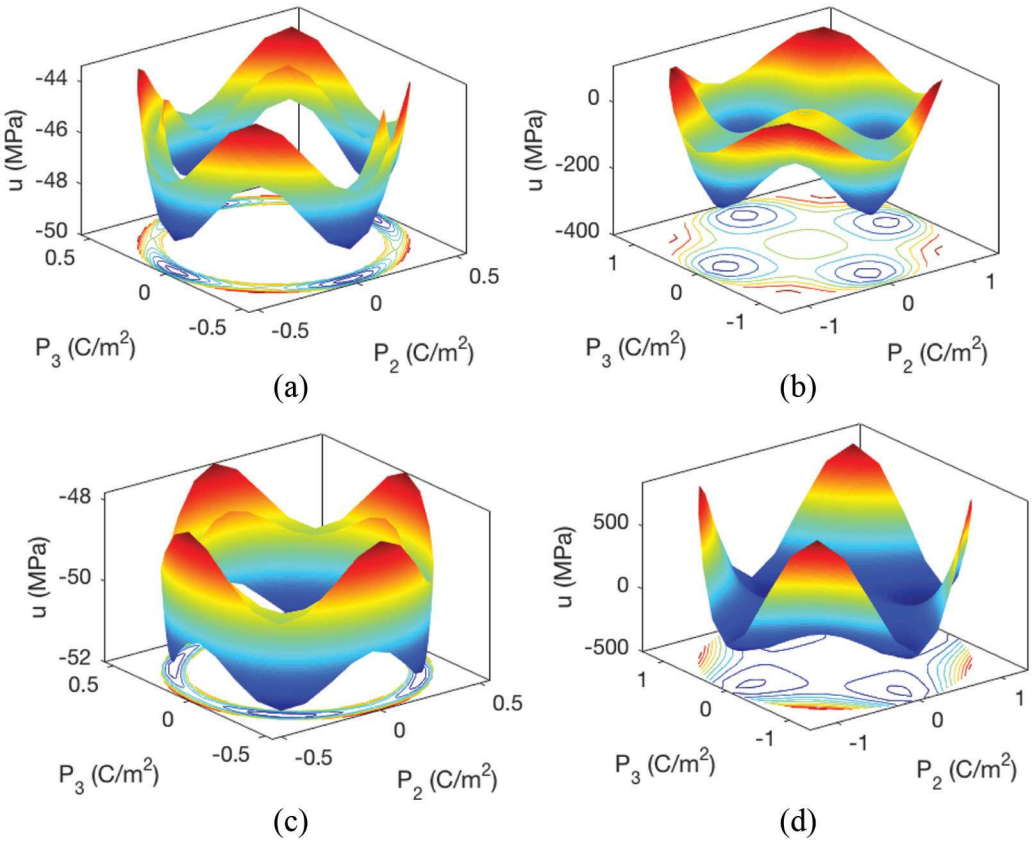

Figure 14. Comparison of sixth-order (a, b) and fourth-order (c, d) energy densities. The Landau energy density (u_L) is plotted in (a) and (c), while the total energy density for the relaxed strain state ($\sigma_{ij} = 0$) is plotted in (b) and (d).

Table 3. Model parameter comparison between this study and Haun et al. (1987). Note that the values of $\bar{\alpha}_{11}$ and $\bar{\alpha}_{12}$ have been augmented so they can be directly compared to the different definitions of the Landau energy function used by Haun et al. (1987). Also note that we have neglected the residual stress in our Landau parameters which may influence α_1 according to electrostriction in equation (17).

Parameter	Current	Haun et al. (1987)	Units
Landau coefficients			
α_1	−389.4	−283.2	MV m/C
$\bar{\alpha}_{11}$	105.7	−72.5	MV m^5/C^3
$\bar{\alpha}_{12}$	2011	750	MV m^5/C^3
α_{111}	61.5	260.6	MV m^9/C^5
α_{112}	−740.8	610	MV m^9/C^5
Electrostrictive coefficients			
Q_{11}	0.073	0.089	m^4/C^2
Q_{12}	−0.015	−0.026	m^4/C^2
Q_{44}	0.029	0.068	m^4/C^2

magnitudes which were not considered for polarization states rotated from the lowest energy spontaneous polarization orientation. Additional details with regard to global sensitivity analysis are given in the complementary Part 2 paper. Since $\alpha_{112} < 0$, the Landau energy grows in the negative direction for large polarization values. Therefore, these parameters for computations such as in phase field methods should be used with caution due to instabilities at large polarization values. Additional comparisons of the Bayesian parameter statistics with experimental fits for lead titanate (Haun et al., 1987) are given in Appendix 1; see Table 3.

We also obtain estimates of the spontaneous strain and polarization by calibrating the Landau energy and electrostrictive stresses. The spontaneous strain predicted by the model using parameters from Tables 1

and 2, in combination with elastic parameters, is $\varepsilon_{33}^S = 7.25\%$ and $\varepsilon_{11}^S = -1.53\%$ for the predicted spontaneous polarization value, $P_3 = P_0 = 0.99\,\mathrm{C/m^2}$. These estimates are based on zero residual stress. Additional predictions of spontaneous strain and polarization that include residual stress are given in Appendix 1. The spontaneous polarization for lead titanate is known to vary widely based on different DFT pseudopotentials (Bilc et al., 2008) as well as experimental measurements (Haun et al., 1987; Lines and Glass, 1977). Haun et al. (1987) estimated the experimental spontaneous polarization near 0 K to be between $0.8 - 0.9\,\mathrm{C/m^2}$. Depending on the DFT exchange and correlation approximation, the computed spontaneous polarization has ranged between $0.78 - 1.40\,\mathrm{C/m^2}$ (Bilc et al., 2008), while several other experimental values range between 0.5 and $1.0\ \mathrm{C/m^2}$ (Lines and Glass, 1977). Using the experimental lattice constant measurements from the literature ($a_T = 3.8995$ Å, $c_T = 4.1552$ Å; Haun et al., 1987) and the extrapolated cubic lattice at room temperature: $\hat{a}_C = 3.96$ Å, we compute the spontaneous strain components ε_{33}^S and ε_{11}^S. These strain components are $\varepsilon_{33}^S = (1/2)[(c_T/\hat{a}_C)^2 - 1] = 5.05\%$ and $\varepsilon_{11}^S = (1/2)[(a/\hat{a}_C)^2 - 1] = -1.52\%$. Extrapolation to near 0 K gave strain estimates of $\varepsilon_{33}^S \simeq 6.25\%$ and $\varepsilon_{11}^S \simeq -1.75\%$ which are in reasonable agreement with Bayesian inferred spontaneous strain estimates. In contrast, the DFT-computed lattice constants ($a = 3.858$ Å and $c = 4.031$ Å; Oates, 2014) give a poorer predictor of strain values $\varepsilon_{11}^s = -2.54\%$ and $\varepsilon_{33}^s = 1.81\%$ using the experimental cubic lattice parameter $\hat{a}_C$ as the reference state.

Our energy function was written as a function of strain and polarization to simplify comparisons between DFT calculations and continuum models using Landau and electrostrictive energy functions. Experimentally, stress is often used as the independent variable (Haun et al., 1987). Therefore, we apply a Legendre transformation in Appendix 1 to provide additional comparisons of our Landau and electrostrictive parameters with measurements taken on lead titanate. Direct comparisons extrapolated to 0 K are given in Table 3. There are notable distinctions between the Bayesian inferred DFT calculations and experimentally determined parameters. These differences could come from multiple sources such as defects, zero-temperature limits, as well as elastic parameters. It was unclear what the experimental elastic parameters were in the study by Haun et al. (1987). These values influence the Landau parameters as described in Appendix 1.

Concluding remarks

Parameters contained within a ferroelectric monodomain model have been analyzed by comparing continuum-scale model approximations to DFT energy and stress calculations. Bayesian statistics have provided information about parameter uncertainty when quantifying the energy landscape over a relatively broad range of the polarization space. Previous analysis that considered changes in energy along the spontaneous polarization direction (Oates, 2014) showed relatively low uncertainty in predictions of energy and stress. Here parameter uncertainty is found to be larger during polarization rotation as highlighted by the shear-related constitutive parameter posterior densities; see Figures 6 and 10. The parameter uncertainty is propagated through the continuum model to quantify prediction intervals of energy and stress along different thermodynamic paths as illustrated in Figures 9 and 13. The larger uncertainty during polarization rotation is believed to manifest at the atomic scale when approximating the motion of multiple atoms within a unit cell in terms of a single polarization vector along the directions not aligned with the spontaneous polarization. Increased parameter sensitivity at larger polarization that is rotated from the spontaneous orientation is also expected to potentially reduce the uncertainty of α_{112}. This is further discussed in the complementary Part 2 paper on global sensitivity.

It is also important to point out the parameter estimation differences in the fourth- and sixth-order Landau energy functions. As shown in Table 1, the inclusion of the sixth-order terms α_{111} and α_{112} influences the shape of the energy surface under zero strain. First, the sign of the fourth-order coefficient α_{12} changes when using either a fourth- or a sixth-order model. Second, Figure 7 illustrates parameter correlation between the pairs $(\alpha_{11}, \alpha_{111})$ and $(\alpha_{12}, \alpha_{112})$. This parameter correlation points to the important coupling between fourth- and sixth-order terms. Caution should be used when freezing higher order terms as a result of perceived lower sensitivity. Quantifying the global sensitivity of these different parameters can provide further insights into their importance and should be done in parallel with Bayesian statistics to keep the most relevant model parameters without introducing unnecessary random parameters that would otherwise create computational inefficiencies. In the cases where correlation exist, parameter sensitivity rankings must account for this effect which is discussed in more detail in the Part 2 paper on new global sensitivity analysis techniques and applications on ferroelectric models. This sign change in estimating α_{12} is important because it predicts a different ferroelectric phase (e.g. rhombohedral versus tetragonal) as illustrated in Figure 14. However, this is only relevant in the constrained strain state. In the relaxed stress state, both the fourth- and sixth-order models estimate the correct tetragonal phase due to the additional effect of electrostriction and elastic energy which is consistent with other homogenized energy models based on DFT results (King-Smith and Vanderbilt, 1994).

Acknowledgements

The research of P.M. and W.S.O. was supported in part by the NSF Grant CDS&E-1306320 Collaborative Research CDS&E, whereas the research of L.L. and R.C.S. was supported in part by the NSF Grant CDS&E-1306290. W.S.O. appreciates preliminary DFT calculations conducted by Justin Collins. Any opinions, findings, and conclusions or recommendations expressed in this publication are those of the authors and do not necessarily reflect the views of the funding sponsors.

Declaration of conflicting interests

The author(s) declared no potential conflicts of interest with respect to the research, authorship, and/or publication of this article.

Funding

The author(s) disclosed receipt of the following financial support for the research, authorship, and/or publication of this article: The research of LL was supported in part by the National Science Foundation under Grant No. DGE-163 3587.

ORCID iD

William S Oates https://orcid.org/0000-0003-4259-5180

References

Bilc D, Orlando R, Shaltaf R, et al. (2008) Hybrid exchange-correlation functional for accurate prediction of the electronic and structural properties of ferroelectric oxides. *Physical Review B* 77(16): 165107.

Cao W and Cross L (1991) Theory of tetragonal twin structures in ferroelectric perovskites with a first-order phase transition. *Physical Review B* 44(1): 5–12.

Cattafesta LN III and Sheplak M (2011) Actuators for active flow control. *Annual Review of Fluid Mechanics* 43: 247–272.

Cohen RE (1992) Origin of ferroelectricity in perovskite oxides. *Nature* 358(6382): 136–138.

Frederiksen SL, Jacobsen KW, Brown KS, et al. (2004) Bayesian ensemble approach to error estimation of interatomic potentials. *Physical Review Letters* 93(16): 165501.

Gonze X, Amadon B, Anglade PM, et al. (2009) ABINIT: first-principles approach to material and nanosystem properties. *Computer Physics Communications* 180(12): 2582–2615.

Haario H, Laine M, Mira A, et al. (2006) DRAM: efficient adaptive MCMC. *Statistics and Computing* 16(4): 339–354.

Haario H, Saksman E, Tamminen J, et al. (2001) An adaptive Metropolis algorithm. *Bernoulli* 7(2): 223–242.

Haun MJ, Furman E, Jang S, et al. (1987) Thermodynamic theory of PbTiO3. *Journal of Applied Physics* 62(8): 3331–3338.

Hu Z, Smith RC, Burch N, et al. (2014) A modeling and uncertainty quantification framework for a flexible structure with macrofiber composite actuators operating in hysteretic regimes. *Journal of Intelligent Material Systems and Structures* 25(2): 204–228.

Huber J, Fleck N, Landis C, et al. (1999) A constitutive model for ferroelectric polycrystals. *Journal of the Mechanics and Physics of Solids* 47(8): 1663–1697.

Jaffe B (2012) *Piezoelectric Ceramics*, vol. 3. New York: Elsevier.

King-Smith R and Vanderbilt D (1994) First-principles investigation of ferroelectricity in perovskite compounds. *Physical Review B* 49(9): 5828.

Kowalewsky O (2004) Theory of complex lattice quasi-continuum and its application to ferroelectrics. PhD Thesis, California Institute of Technology, Pasadena, CA.

Laine M (2013) DRAM. Available at: http://helios.fmi.fi/~lainema/dram/

Lines ME and Glass AM (1977) *Principles and Applications of Ferroelectrics and Related Materials*. Oxford: Oxford university press.

Malvern LE (1969) *Introduction to the Mechanics of a Continuous Medium*. London: Monograph and Prentice-Hall, Inc.

Oates W (2014) A quantum informed continuum model for ferroelectric materials. *Smart Materials and Structures* 23(10): 104009.

Payne MC, Teter MP, Allan DC, et al. (1992) Iterative minimization techniques for ab initio total-energy calculations: molecular dynamics and conjugate gradients. *Reviews of Modern Physics* 64(4): 1045.

Resta R (1994) Macroscopic polarization in crystalline dielectrics: the geometric phase approach. *Reviews of Modern Physics* 66(3): 899.

Ruglovsky JL, Li J, Bhattacharya K, et al. (2006) The effect of biaxial texture on the effective electromechanical constants of polycrystalline barium titanate and lead titanate thin films. *Acta Materialia* 54(14): 3657–3663.

Shirane G, Pepinsky R and Frazer B (1956) X-ray and neutron diffraction study of ferroelectric PbTiO2. *Acta Crystallographica* 9(2): 131–140.

Smith RC (2005) *Smart Material Systems: Model Development*. Philadelphia, PA: SIAM.

Smith RC (2013) *Uncertainty Quantification: Theory, Implementation, and Applications*, vol. 12. Philadelphia, PA: SIAM.

Su Y and Landis CM (2007) Continuum thermodynamics of ferroelectric domain evolution: theory, finite element implementation, and application to domain wall pinning. *Journal of the Mechanics and Physics of Solids* 55(2): 280–305.

Vanderbilt D (2004) First-principles theory of polarization and electric fields in ferroelectrics. *Ferroelectrics* 301(1): 9–14.

Völker B, Marton P, Elsässer C, et al. (2011) Multiscale modeling for ferroelectric materials: a transition from the atomic level to phase-field modeling. *Continuum Mechanics and Thermodynamics* 23(5): 435–451.

Appendix 1

The following relations provide a comparison of experimental energy functions in terms of stress and polarization with the results given in this article. The Legendre transformation is presented and several relations describing spontaneous strain and polarization are derived.

Legendre transformation from strain to stress

Haun et al. (1987) define the energy functions with respect to stress and polarization. For self-consistent comparison of Landau and electrostrictive parameters, the model in equation (1) is defined using stress and polarization as the independent variables. Given the non-linearities of the Landau energy function, we start with the stress defined as

$$\sigma_{ij} = \frac{\partial u}{\partial \varepsilon_{ij}} = c_{ijkl}\varepsilon_{kl} - q_{ijkl}P_kP_l + \sigma^R_{ij}.$$

This can be rearranged to find the strain as

$$\varepsilon_{ij} = s_{ijkl}\left(\sigma_{kl} - \sigma^R_{kl}\right) + s_{ijkl}q_{klmn}P_mP_n. \tag{16}$$

Recall from Malvern (1969) that the compliance tensor s_{ijkl} is the inverse of the stiffness tensor c_{ijkl}.

Substituting equation (16) into equations (2), (4), and (5) yields the updated expressions for u_M, u_C, and u_R, respectively

$$\begin{aligned} u_M &= \frac{1}{2}\left[s_{rsmn}\sigma^M_{rs}\sigma^M_{mn} + 2s_{rsmn}q_{rsab}\sigma^M_{mn}P_aP_b \right. \\ &\quad \left. + s_{rscd}q_{rsab}q_{cdef}P_aP_bP_eP_f\right] \\ u_C &= -q_{ijkl}s_{ijmn}P_kP_l\sigma^M_{mn} \\ &\quad -q_{ijkl}s_{ijrs}q_{rsmn}P_mP_nP_kP_l \\ u_R &= \left(s_{ijkl}\sigma^M_{kl} + s_{ijrs}q_{rskl}P_kP_l\right)\left(\sigma^R_{ij}\right) \end{aligned} \tag{17}$$

where we have introduced the relation $\sigma^M_{ij} = \sigma_{ij} - \sigma^R_{ij}$. The converted model in equation (17) is not a direct match to Haun et al. (1987); however, an equivalent set of model parameters are determined and have been compared in Table 3. The electrostrictive coefficients result from the expansion of

$$\begin{aligned} &q_{ijkl}s_{ijmn} \rightarrow \\ &Q_{11} = q_{11}s_{11} + 2q_{12}s_{12} \\ &Q_{12} = q_{11}s_{12} + q_{12}s_{11} + q_{12}s_{12} \\ &Q_{44} = 2q_{44}s_{44} \end{aligned} \tag{18}$$

Two additional coefficients that arise as a result of the transformation are

$$\begin{aligned} &\frac{1}{2}q_{ijkl}s_{ijrs}q_{rsmn} \rightarrow \\ &\beta_1 = \frac{q^2_{11}s_{11}}{2} + q^2_{12}s_{11} + q^2_{12}s_{12} + 2q_{11}q_{12}s_{12} \\ &\beta_2 = q^2_{11}s_{12} + q^2_{12}s_{11} + 3q^2_{12}s_{12} + 2q_{11}q_{12}s_{11} \\ &\quad + 2q_{11}q_{12}s_{12} + 2q^2_{44}s_{44} \end{aligned} \tag{19}$$

These two β_i coefficients scale the fourth-order polarization terms, so their values influence α_{11} and α_{12} as follows.

The Landau polarization energy defined in equation (3) can be defined in two distinct ways, which can potentially shift the value of α_{12}. We followed Cao and Cross (1991) using α_{11} to scale the term $(P^2_1 + P^2_2 + P^2_3)^2$. Alternatively, the Landau function can be defined such that α_{11} scales the term $P^4_1 + P^4_2 + P^4_3$ (Haun et al., 1987; Völker et al., 2011). To directly compare the parameters, we expand the polynomial $(P^2_1 + P^2_2 + P^2_3)^2 = (P^4_1 + P^4_2 + P^4_3) + 2(P^2_2P^2_3 + P^2_1P^2_3 + P^2_1P^2_2)$ and combine like parameters. Therefore, in Table 3 we report the values $\bar{\alpha}_{11} = \alpha_{11} - \beta_1$ and $\bar{\alpha}_{12} = 2\alpha_{11} + \alpha_{12} - \beta_2$ to directly compare fourth-order parameters reported in Haun et al. (1987) with our mean Bayesian parameter estimations.

Spontaneous polarization and strain

Expansion of the free energy via variational methods gives rise to the static equilibrium conditions with respect to polarization and strain. The condition for static equilibrium with regard to polarization is

$$\frac{\partial}{\partial x_j}\left(\frac{\partial u}{\partial P_{i,j}}\right) - \frac{\partial u}{\partial P_i} = 0, \quad (i,j = 1,2,3) \tag{20}$$

The stress in the material is found by taking the derivative of the energy function with respect to strain, and so the equilibrium constraint is

$$\sigma_{ij,j} = \frac{\partial}{\partial x_j}\left(\frac{\partial u}{\partial \varepsilon_{ij}}\right) = 0, \quad (i,j = 1,2,3). \tag{21}$$

The divergence of stress should be zero for systems at static equilibrium.

The monodomain, that is, region of uniform polarization, energy is a function of temperature, which can be described by the phenomenological parameters in equations (2), (3), and (4). All physical quantities are uniform in space, so equations (20) and (21) reduce to

$$\frac{\partial u}{\partial P_i} = 0, \ \sigma_{ij} = 0 \tag{22}$$

Note that the condition on stress assumes that no external stresses are being applied. Assuming that all the polarization is oriented in the x_3 direction, one is left with the following system of equations

$$\begin{aligned} \frac{\partial u}{\partial P_3} &= 2\alpha^+_1P_3 + 4\alpha_{11}P^3_3 + 6\alpha_{111}P^5_3 = 0 \\ \frac{\partial u}{\partial \varepsilon_{11}} &= c_{11}\varepsilon_{11} + c_{12}(\varepsilon_{22} + \varepsilon_{33}) - q_{12}P^2_3 + \sigma^R_{11} = 0 \\ \frac{\partial u}{\partial \varepsilon_{22}} &= c_{11}\varepsilon_{22} + c_{12}(\varepsilon_{11} + \varepsilon_{33}) - q_{12}P^2_3 + \sigma^R_{22} = 0 \\ \frac{\partial u}{\partial \varepsilon_{33}} &= c_{11}\varepsilon_{33} + c_{12}(\varepsilon_{11} + \varepsilon_{22}) - q_{11}P^2_3 + \sigma^R_{33} = 0 \end{aligned} \tag{23}$$

where $\alpha^+_1 = \alpha_1 + q_{11}\varepsilon_{33} + q_{12}(\varepsilon_{11} + \varepsilon_{22})$. For temperatures well below the Curie temperature, the solution for polarization in a monodomain system is

$$P_3 = P_0 = \left(\frac{-\alpha'_{11} + \left(\alpha'_{11}2 - 3\alpha_1^*\alpha_{111}\right)^{1/2}}{3\alpha_{111}} \right)^{1/2} \quad (24)$$

where α_1^* and α'_{11} are

$$\begin{aligned} \alpha_1^* &= \alpha_1 + \frac{1}{\hat{c}_{11}\hat{c}_{22}}\left[(c_{11}q_{12} - c_{12}q_{11})\left(\sigma_{11}^R + \sigma_{22}^R\right)\right. \\ &\left. + (c_{11}q_{11} + c_{12}(q_{11} - 2q_{12}))\sigma_{33}^R\right] \\ \alpha'_{11} &= \alpha_{11} \\ &+ \frac{4c_{12}q_{11}q_{12} - q_{11}^2(c_{11} + c_{12}) - 2c_{11}q_{12}^2}{2\hat{c}_{11}\hat{c}_{22}} \end{aligned} \quad (25)$$

Recall that the results for spontaneous strain and polarization given in the end of section "Bayesian inference results" were computed for zero residual stress. When including our mean values for residual stress from Table 2, we find a numerical solution for the spontaneous polarization and strain to be $P_0 = 1.1\,\mathrm{C/m^2}$, $\varepsilon_{11} = \varepsilon_{22} = -1.1\%$, and $\varepsilon_{33} = 9.3\%$.